

PCCP

Accepted Manuscript



This is an *Accepted Manuscript*, which has been through the Royal Society of Chemistry peer review process and has been accepted for publication.

Accepted Manuscripts are published online shortly after acceptance, before technical editing, formatting and proof reading. Using this free service, authors can make their results available to the community, in citable form, before we publish the edited article. We will replace this *Accepted Manuscript* with the edited and formatted *Advance Article* as soon as it is available.

You can find more information about *Accepted Manuscripts* in the [Information for Authors](#).

Please note that technical editing may introduce minor changes to the text and/or graphics, which may alter content. The journal's standard [Terms & Conditions](#) and the [Ethical guidelines](#) still apply. In no event shall the Royal Society of Chemistry be held responsible for any errors or omissions in this *Accepted Manuscript* or any consequences arising from the use of any information it contains.

Electrical conductivity and thermopower of (1-x) BiFeO₃ – x Bi_{0.5}K_{0.5}TiO₃ (x=0.1, 0.2) ceramics near the ferroelectric to paraelectric phase transition

Cite this: DOI: 10.1039/x0xx00000x

E.T. Wefring,^a M.-A. Einarsrud^a and T. Grande^{a,*}

Received 00th January 2012,
Accepted 00th January 2012

DOI: 10.1039/x0xx00000x

www.rsc.org/

Ferroelectric BiFeO₃ has attractive properties such as high strain and polarization, but wide application of bulk BiFeO₃ has been hindered due to high leakage currents and high coercive field. Here, we report on the thermal behaviour of the electrical conductivity and thermopower of BiFeO₃ substituted with 10 and 20 mol% Bi_{0.5}K_{0.5}TiO₃. A change from p-type to n-type conductivity in these semi-conducting materials was demonstrated by the change in the sign of the Seebeck coefficient and the change in the slope of the isothermal conductivity versus partial pressure of O₂. A minimum in the isothermal conductivity was observed at ~10⁻² bar O₂-pressure for both solid solutions. The strong dependence of the conductivity with the partial pressure of O₂ was rationalized by a point defect model describing qualitatively the conductivity involving oxidation/reduction of Fe³⁺, the dominating oxidation state of Fe in stoichiometric BiFeO₃. The ferroelectric to paraelectric phase transition of 80 and 90 mol% BiFeO₃ was observed at 648±15 and 723±15 °C respectively by differential thermal analysis and confirmed by dielectric spectroscopy and high temperature powder X-ray diffraction.

1. Introduction

Legislations, prohibiting the use of lead in electronics, have been passed by the European Union and other countries due to environmental concerns.¹ Lead-free piezoelectric materials have therefore received significant interest in recent years to replace the state of the art lead-containing piezoelectric Pb(Zr,Ti)O₃ (PZT).² Bismuth containing perovskite-based materials are among the most promising lead-free alternatives, and among these bismuth ferrite, BiFeO₃ (BFO), and bismuth potassium titanate, Bi_{0.5}K_{0.5}TiO₃ (BKT), have been investigated intensively.^{2,3} BFO with a rhombohedral structure has attracted tremendous interest due to its multiferroic properties^{3,4}, including the potential as a ferro- or piezoelectric material with high polarization, lattice strain and Curie temperature (T_C, 830 °C), the latter being important for high temperature applications.⁵⁻⁷ The prospects of applying BFO is though hampered by parasitic secondary phases formed during synthesis^{8, 9}, high coercive electric field and high dielectric losses stemming from conductivity.^{3,10} BKT is a tetragonal ferroelectric which shows a relatively high piezoelectric constant and T_C (380 °C).^{11,12} Challenges with fabrication of dense BKT ceramics have been reported¹³ but dense single phase materials can be obtained by solid state synthesis.¹⁴ BKT is also an important constituent in solid solution systems, which may possess a morphotropic phase boundary (MPB) similar to the one known for PZT.²

Solid solutions of BFO and BKT have recently been investigated due to a possible MPB.^{12,13,15-20} Doping BFO with BKT suppress the formation of the parasitic phases well known in pure BFO and phase pure BFO-BKT materials are obtained by conventional solid state synthesis.^{8, 15} BFO-BKT materials are isostructural with BFO at high BFO content. A maximum in the dielectric and electromechanical

properties is reported at 25 mol% BFO, and the piezoelectric properties such as electric field induced polarization and strain decreases towards a high BFO content^{15, 17} probably due to the high coercive electric field and dielectric loss of BFO relative to that of BKT.^{5,13} Morozov et al. have recently shown that the conductivity of BFO-BKT materials can be reduced by annealing in inert atmosphere improving the electromechanical performance.²⁰ A Maxwell-Wagner type relaxation in BFO-BKT, coupled to the electrical conductivity and point defects, has also been reported.²¹

One of the main challenges with BFO is the high electrical conductivity giving rise to dielectric loss.³ Pure and acceptor substituted BFO shows the characteristics of p-type conductivity in air, relating conductivity to the presence of Fe⁴⁺.²²⁻²⁶ The conductivity of 0.7BFO-0.3BKT can be manipulated by thermal treatment in oxidizing or inert atmosphere.^{20,21} Aliovalent substitution of Fe³⁺ with e.g. Ti⁴⁺ and Ni²⁺ on the perovskite B site has profound effect on the conductivity of BFO²⁷⁻²⁹ where tetravalent cations reduce the conductivity and divalent cations increase the conductivity. Particularly, substitution with Ti has shown great promise to reduce the conductivity of BFO.^{27,29,30} The observed effects are discussed in relation to the presence of Fe²⁺ and oxygen vacancies, and coulometric titration has shown that 2 mol% Fe²⁺ can be present in BFO before decomposition of BFO occurs at reducing conditions.³¹ However, the effect of presence of Fe²⁺ on the conductivity of bulk BFO has yet to be established.

Evaporation of Bi₂O₃ during synthesis increases the point defect concentration in BFO materials.¹⁰ Bi vacancies can be charge compensated by oxygen vacancies or oxidation of Fe³⁺. The presence of multivalent Fe will strongly influence the electrical conductivity of BFO, as it depends on small polaron hopping.^{27,32,33} P-type (in air) and n-type (reducing conditions) semiconductor

behaviour has previously been reported for several related Fe-containing perovskites, including $\text{La}_{1-x}\text{Sr}_x\text{FeO}_{3-\delta}$ ³⁴⁻³⁶ and LnFeO_3 (Ln = Pr, Nd, Sm, Eu and Gd)^{37,38}. In these materials the electronic conductivity is strongly linked to polaron hopping and the oxidation state of Fe, which is strongly dependent on the partial pressure of oxygen ($p(\text{O}_2)$).

Here we report on the electrical conductivity and thermopower of BFO substituted with 10 and 20 mol% BKT. This solid solution was chosen as model systems to obtain physical insight in the electrical conductivity of BFO-based materials, avoiding the influence of secondary phases typically found in pure bulk BFO. We provide experimental evidence for that the conductivity changes from p-type to n-type when going from oxidizing to inert conditions, demonstrating clearly for the first time why the electrical conductivity can be minimized by annealing in controlled partial pressure of oxygen. The ferroelectric phase transition of the materials is investigated by high temperature X-ray diffraction, dielectric spectroscopy/electrical conductivity and differential thermal analysis. Finally, a conventional point defect model is applied to describe the dependence of the electrical conductivity with $p(\text{O}_2)$.

2. Experimental

Ceramics with composition $(1-x)\text{BiFeO}_3-x\text{Bi}_{0.5}\text{K}_{0.5}\text{TiO}_3$ ($x = 0.2, 0.1$, denoted 0.8BFO and 0.9BFO) were prepared by solid state synthesis as reported by Morozov et al.¹⁷ Stoichiometric amounts of dried Bi_2O_3 (Aldrich, 99.9%), K_2CO_3 (Aldrich, 99.99%), TiO_2 (Aldrich, 99.9%) and Fe_2O_3 (Aldrich, 99.999%) precursors were mixed and ball milled in isopropanol (18 h). The precursor mixture was calcined (5 h) in air at 820 °C ($x = 0.2$) and 800 °C ($x = 0.1$). The calcined powders were ball milled in isopropanol (18 h), dried and sieved (250 μm sieve), and further pressed into pellets/bars by uniaxial pressing and cold isostatic pressing (200 MPa). The samples were sintered in air (2 h) covered by sacrificial powder at 1010 °C ($x = 0.2$) and 980 °C ($x = 0.1$). Powders for X-ray diffraction (XRD) were prepared by crushing the sintered pellets followed by annealing the powders above the Curie temperature.

The density of the materials was measured by Archimedes method (ISO 5017:1998(E)) and the relative density was calculated with respect to the crystallographic density determined by XRD. The grain size was determined by the intercept method from polished and thermally etched samples (880 °C, 5 min) using a scanning electron microscope (SEM; Hitachi S-3400N).

Electronic conductivity was measured using a direct current (DC) four-point method, as previously described by Wærnhus et al.³⁹ The surface of sintered bars was polished using a grade #220 silicon carbide grinding paper to dimensions of about 22 x 4.5 x 3 mm. A constant voltage was applied over the current circuit and the distance between the voltage electrodes on the sample was 5 mm. Pt-paste was used to ensure sufficient contact between the current electrodes and the sample. The DC electrical conductivity was measured at 700, 750 and 800 °C at a constant $p(\text{O}_2)$. The temperature was reduced to 650 °C before a new $p(\text{O}_2)$ was introduced. The conductivity relaxation was observed and the conductivity was allowed to stabilize at the specific conditions before the temperature or the atmosphere was altered. The temperature was measured by an S-type thermocouple and the partial pressure of oxygen (O_2 , 0.2, 0.02, 0.002, N_2) was controlled by mixing O_2 and N_2 (Yara Praxair, 5.0) at flow rates of 50, 250 or 500 mL/min.

The Seebeck-coefficient (Q) was measured at 650, 700, 750 and 800 °C using a ProboStat™ setup (NorECs AS) in a vertical tubular furnace with a vertical bar analogous to the bar used to measure the electrical conductivity. The temperature gradient was measured by two S-type thermocouples (20-25 °C) and the voltage across the

sample was measured using Pt-electrodes. The atmosphere was varied by manual flow control of O_2 , N_2 and synthetic air (Yara Praxair, 5.0).

Dielectric properties were investigated in synthetic air (Yara Praxair, 5.0) using a frequency analyzer (Alpha-A High Performance Frequency Analyser, Novocontrol Technologies) connected to a ProboStat™ setup in a vertical tubular furnace. Gold electrodes were sputtered onto ground and cleaned faces of a sintered pellet, and measurements were performed during continuous heating/cooling (2 °C/min) every 30 second at frequencies 1-10⁶ Hz. The electroded sample was first heated/cooled to/from 400 °C to remove Maxwell-Wagner contributions to the permittivity.²¹ The reported data is from a 2nd heating cycle to 720 °C and 800 °C for 0.8BFO and 0.9BFO, respectively.

High temperature X-ray diffraction (HTXRD) was performed with a θ - θ Bruker D8 ADVANCE diffractometer utilizing Cu K_α radiation and a VANTEC-1 position sensitive detector. Powders for investigation were contained within an alumina sample holder and heated using a radiant heater mounted within an MRI Physikalische Geräte GmbH high temperature camera. Calibration of the system against an Al_2O_3 standard gave an estimated temperature error of ± 15 °C. Diffraction patterns were collected from room temperature to 760 °C (every 50 degrees up to 510 °C, every 10 degrees above 510 °C), across an angular range 20-75° 2θ with a step size of 0.016° (1 second/step). Lattice parameters for each diffraction pattern were determined by Pawley fitting using the Topas software.⁴⁰ A hexagonal model ($R3c$) was adopted below the Curie temperature and a cubic model ($Pm\bar{3}m$) above, as previously described for BiFeO_3 and Mn-doped BiFeO_3 .^{41,42} Peak shapes were described using a Pseudo-Voigt model (TCHZ) and a Chebychev polynomial background function was used. Sample displacement and lattice parameters were refined for each temperature.

Differential thermal analysis (DTA) was used to determine the ferroelectric to paraelectric phase transition (STA 449 C, Netzsch). The powder used for DTA was prepared the same way as the powder for XRD, from the same sintered pellet. The powder was packed in alumina crucibles and heated to 750 °C (0.8BFO) and 800 °C (0.9BFO) at 10 °C/min in synthetic air (30 mL/min). The samples were kept at T_{max} for 5 minutes before cooling.

3. Results

Dense ($97 \pm 1\%$ of theoretical density) and phase pure ceramics with compositions 0.8BFO and 0.9BFO were successfully prepared by conventional solid state synthesis. No secondary phases could be observed in the sintered specimens by X-ray diffraction as well as by electron microscopy in agreement with previous work.¹⁷ The microstructure of the dense and single phase materials, shown in Figure 1, is relatively homogeneous with submicron grain size (Table 1). No evidence for the presence of any secondary phases could be observed by SEM/back scattered electrons. The room temperature unit cell parameters determined from the diffraction pattern (not shown) are given in Table 1.

The DC electrical conductivity of 0.8BFO and 0.9BFO is shown as a function of temperature and $p(\text{O}_2)$ in Figures 2a and 2b, respectively. The conductivity increases with increasing BFO content, reflecting a higher conductivity of BFO relative to BKT,^{42,43} and it increases with increasing temperature in line with a semiconductor behaviour. A distinct minimum in the isothermal conductivity versus $\log p(\text{O}_2)$, typical for the p-type to n-type transition of oxide semiconductors, is evident for both compositions. P-type conductivity is characteristic for the materials in oxidizing atmosphere, while n-type is typical for inert or reducing conditions. Similar p-type behaviour is observed for Ca-substituted, BiFeO_3 ,²⁶ but the minimum in the conductivity as well as the n-type

conductivity in bulk BFO-materials has not been reported previously.

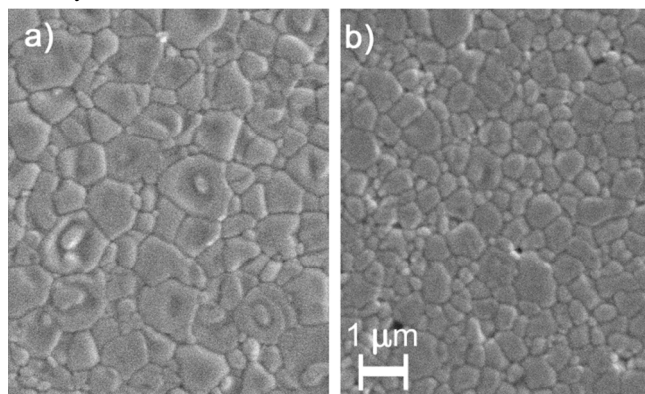


Fig 1 SEM micrographs (secondary electrons) of polished and thermally etched 0.8BFO (a) and 0.9BFO (b) ceramics.

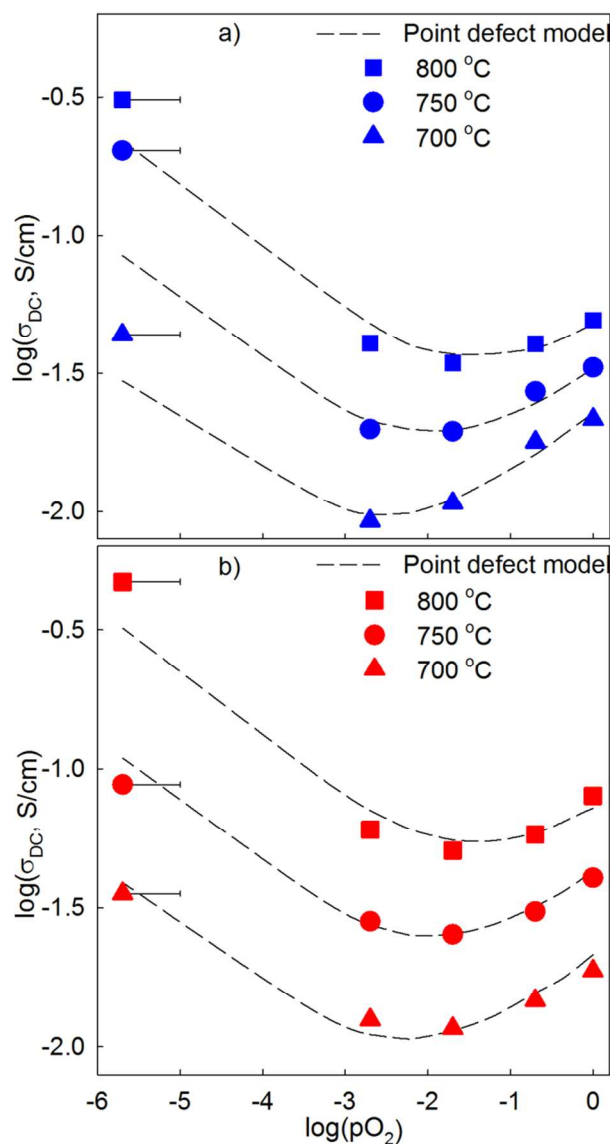


Fig 2 DC conductivity of 0.8BFO (a) and 0.9BFO (b) as a function of $p(\text{O}_2)$ at 700, 750 and 800 °C. The dotted lines are the conductivity calculated by the point defect model introduced in the discussion section. The uncertainty associated with the $p(\text{O}_2)$ in N_2 is shown by error bars.

Table 1 Lattice parameters, grain size and phase transition temperature of 0.8BFO and 0.9BFO

| | | 0.8BFO | 0.9BFO |
|-------------------------------------|------------------------|----------------|----------------|
| Room temperature lattice parameters | a [Å] | 5.591(8) | 5.584(6) |
| | c [Å] | 13.80(6) | 13.840(8) |
| Grain size | [μm] | 0.9 ± 0.05 | 0.6 ± 0.03 |
| Permittivity heating | Temp. of peak max [°C] | 675 ± 15 | - |
| Permittivity cooling | 10 kHz | 620 ± 15 | - |
| Phase transition HTXRD | [°C] | 630 ± 15 | 676 ± 15 |
| DTA heating | Peak onset [°C] | 648 ± 15 | 723 ± 10 |
| | Peak max [°C] | 680 ± 1 | 746 ± 1 |
| DTA cooling | Peak onset [°C] | 641 ± 5 | 743 ± 10 |
| | Peak min [°C] | 619 ± 1 | 713 ± 1 |

While the materials were single phase after sintering, it is worth noting that a Fe/Ti-rich secondary phase was observed on the surface of the materials after the long period of electrical DC conductivity measurement (640 and 770 hours for 0.8BFO and 0.9BFO respectively). The formation of secondary phase on the surface is most likely related to the loss of Bi_2O_3 during the measurements as shown previously for pure BFO.⁴

The Seebeck coefficients in the temperature range 650–800 °C in three different atmospheres, shown in Figure 3, demonstrate clearly the p-type conductivity in air and oxygen and n-type conductivity in inert atmosphere. The negative Seebeck coefficient is to the author's knowledge the first direct evidence for n-type conductivity of bulk BFO-rich materials. The positive Seebeck coefficient for BFO at 650 °C in air has been reported as $\sim 600 \mu\text{V/K}$ in reasonable agreement with the present data. It is clear that the Seebeck coefficient increases with increasing BKT content.⁴⁴

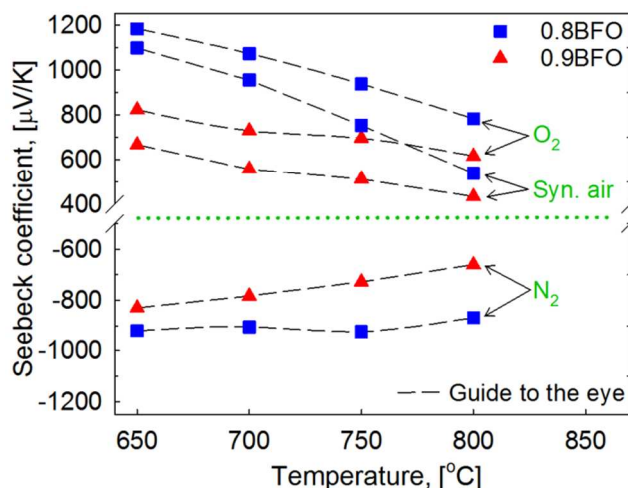


Fig 3 The Seebeck coefficient of 0.8BFO and 0.9BFO as a function of temperature in three different atmospheres.

The real part of the permittivity of 0.8BFO during heating (10 kHz, 100 kHz, 1 MHz) and cooling (10 kHz) in synthetic air is shown in Figure 4a. No temperature dispersion of the maximum

permittivity (ϵ'_{\max}) is observed during heating, pointing to a true ferroelectric phase transition in line with what is previously reported.²¹ The temperature of ϵ'_{\max} is included in Table 1. The shift in the maximum permittivity observed during cooling points to a first order phase transition. Permittivity data for 0.9BFO are not reported due to the high conductivity of this particular material close to the phase transition.

The real part of the AC conductivity (10 kHz) during heating is shown for 0.8BFO and 0.9BFO in Figure 4b. The conductivity increases with temperature and changes slope around 240 °C and in the temperature range of the ferroelectric to paraelectric phase transition for all frequencies. The DC conductivity measured during heating is in good accordance with the data measured at isothermal conditions (Figure 2).

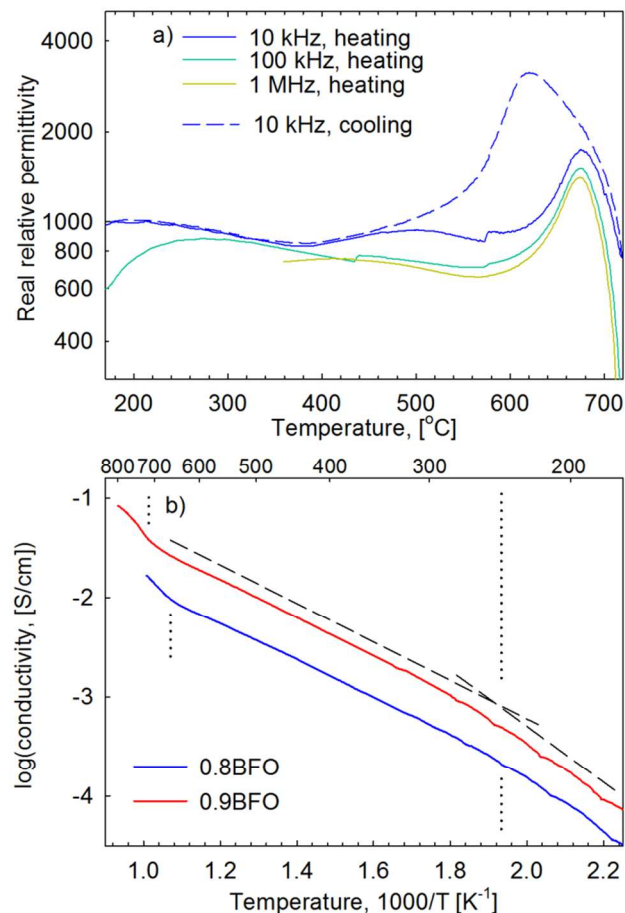


Fig 4 The real permittivity during heating (solid lines) and cooling (dashed line) of 0.8BFO (a) and the real part of the AC conductivity (10 kHz) for 0.8BFO and 0.9BFO during heating (b). In (b), the dashed lines show the slope and dotted lines mark temperature ranges of changing slope. All measurements were performed in synthetic air.

The thermal evolution of the HTXRD diffractograms of 0.8BFO and 0.9BFO is shown in Figure 5a and 5b, respectively. Both materials were indexed to the *R3c* space group from room temperature up to the ferroelectric to paraelectric phase transition temperature. The most pronounced change with temperature is the reduced splitting of the (006) and (202) reflections (insert in Figure 5a and 5b). Above the phase transition the diffraction patterns were indexed using the space group *Pm3m*. Pure BFO is known to be orthorhombic *Pbnm* above T_C ,⁴⁵ but no super reflections due to tilting of the octahedra could be observed and the cubic space group

was therefore used. The phase transition temperature was estimated to 630 ± 15 °C (0.8BFO) and 676 ± 15 °C (0.9BFO) based on the diffraction data (Table 1).

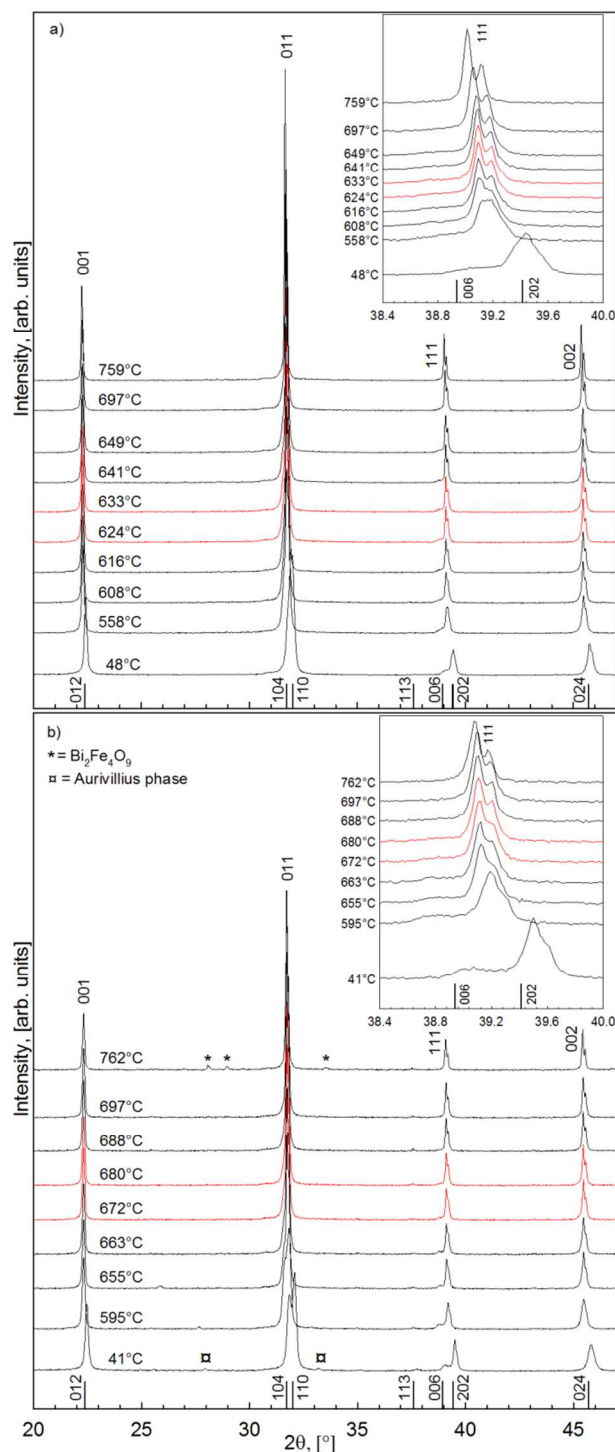


Fig 5 X-ray diffractograms of 0.8BFO (a) and 0.9BFO (b) at selected temperatures. The vertical bars show the reflections with indices for rhombohedral BFO. The Miller indices above the reflections refer to the cubic symmetry at high temperature. The phase transition occurs in the temperature range of the red diffractograms (624 and 633 °C for 0.8BFO, 672 and 680 °C for 0.9BFO). The inset shows the 006/202 diffraction lines in detail. The secondary phase (α) seen at low temperature in 0.9BFO was not present after sintering, but appeared after thermal annealing above T_C prior to the HTXRD analysis.

The thermal evolution of the pseudo cubic unit cell parameters for 0.9BFO and 0.8BFO is compared to the lattice parameters of pure BFO in Figure 6.⁴⁶ The unit cell parameters are normalized as follows; $a_{pc} = 2^{-1/2} a_h$ and $c_{pc} = 12^{-1/2} c_h$, where pc and h refer to pseudo cubic and hexagonal, respectively. The thermal expansion of a_{pc} and c_{pc} is close to linear far below the phase transition. A strong contraction of the c-axis is evident close to T_C as reported for BiFeO₃ due to the ferroelectric to paraelectric phase transition.^{45, 46} The unit cell volume is discontinuous at the phase transition (insert Figure 6) demonstrating a 1st order phase transition as reported for BFO.^{45, 46}

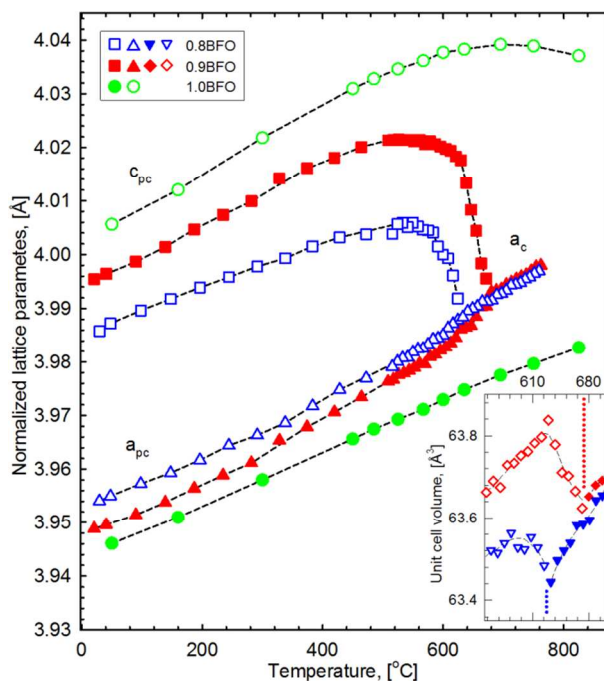


Fig 6 Refined and pseudo cubic (normalized) lattice parameters for 0.8BFO, 0.9BFO and BFO (1.0BFO).⁴⁶ Dashed lines serve as a guide to the eye. The inset shows unit cell volume below (open symbols) and above (filled symbols) the ferroelectric phase transition (marked by dotted lines).

The phase transition of 0.8BFO and 0.9BFO observed by DTA is presented in Figure 7. An endothermic peak upon heating and an exothermic peak during cooling are clearly evident. The temperature for the onset of the peaks is included in Table 1 along with the temperature of the peak maximum/minimum. The hysteresis between the heating and cooling curves confirms the 1st order of the phase transition.

4. Discussion

The qualitative behaviour of the electrical conductivity at different $p(O_2)$ for 0.8BFO and 0.9BFO show great similarities to the properties reported for similar Fe-based perovskite materials.³⁴⁻³⁸ The electrical conductivity of these materials has previously been modelled with success by a mass action type treatment of point defect equilibria. A mass action type model adapted for 0.8BFO and 0.9BFO is introduced here based on the approach presented by Mizusaki et al.³⁶ for LaFeO₃. The substitution of K⁺ into the A-site and Ti⁴⁺ into the B-site of BFO can be seen as acceptor and donor substitution, respectively, resulting in K_{Bi}^{\bullet} and Ti_{Fe}^{\bullet} as point defects using the Kröger-Vink notation. These two point defects are charge balanced by the K:Ti substitution ratio of 1:2, and can therefore be

neglected to a first approximation. The point defect chemistry in $(1-x)BFO - xBKT$ can, analogous to LaFeO₃, be described by a model based on 5 equations. First, the point defect equilibria related to the volatility of Bi₂O₃ (1), the principle of electro neutrality (2) and the mass balance of Fe (3) are defined.

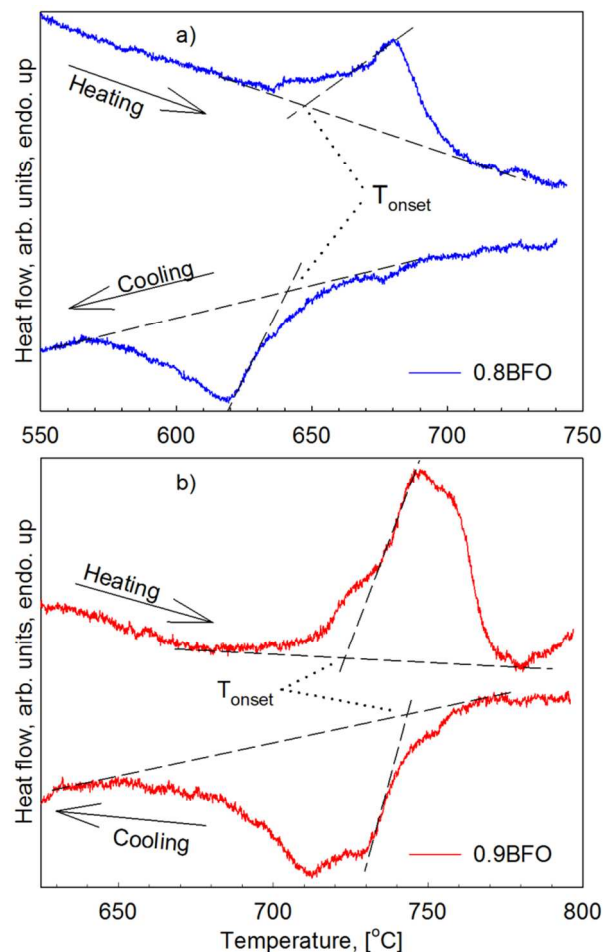
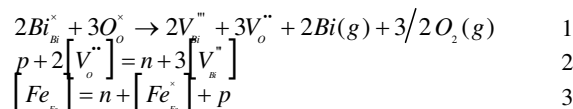
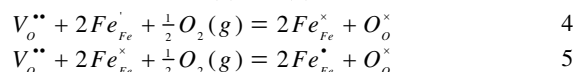


Fig 7 DTA heat flow signal for 0.8BFO (a) and 0.9BFO (b). The black lines give the determination of T_{onset} .



Here, V_{Bi}^{\bullet} is Bi vacancy, V_o^{\bullet} is an oxygen vacancy and n and p are concentrations of electrons and holes, respectively. The electrons and holes correspond to the concentration of Fe²⁺ and Fe⁴⁺ respectively, where the valence of Fe is connected to $p(O_2)$ through the oxidation reactions (4) and (5).



The total electrical conductivity (σ_{tot}) of the material is described by Equation (6)

$$\sigma_{tot} = \sigma_{ion} + \sigma_e + \sigma_h \approx N_v n e \mu_e + N_v p e \mu_h \quad 6$$

where σ_{ion} is the ionic conductivity, σ_e and σ_h is the contribution from electrons and holes, respectively, N_v is the density of states, e is the charge of an electron, and μ_e and μ_h are the mobility of electrons and holes respectively. For the further calculations it is assumed that $\sigma_{ion} \ll \sigma_e, \sigma_h$. At the $p(O_2)$ corresponding to the minimum in the

conductivity, see Figure 2a and 2b (σ_{\min}), the contribution from electrons and holes can be expressed by Equation (7)

$$\frac{\sigma_{\min}}{2} = \sigma_h(\sigma_{\min}) = \sigma_e(\sigma_{\min}) = (K_i')^{0.5} \quad 7$$

where $K_i' = \sigma_e \cdot \sigma_h$. A combination of Equations (6) and (7) allows for determining $\sigma_h(p(O_2))$ and $\sigma_e(p(O_2))$. Following this, Equation (6) can be used to determine n and p . The mobility of electrons and holes (Table 2) were adjusted to fit the model, based on corresponding data reported for LaFeO_3 .²³

Accurate data on the extent of A-site cation deficiency due to evaporation of Bi_2O_3 (and/or K_2O) during solids state reaction and sintering has so far not been determined, but accurate data on the cation non-stoichiometry are critical for further development of the model. Here, an assumption that $[V_{\text{Bi}}] = 0.01$ was introduced based on preliminary data.⁴⁷

The optimized enthalpies for reaction s 4 and 5 are listed in Table 2. The Gibbs energy was estimated by assuming that the entropy of the reactions is equal to -130 kJ/mol as argued by Bakken et al.⁴⁸

The model for the conductivity, shown by the dashed lines in Figure 2, shows that the dominating charge carriers in 0.8BFO and 0.9BFO are electrons or holes. While a positive Seebeck coefficient was measured in oxygen and air, a negative value was measured at low $p(O_2)$ proving the change of the sign of the main charge carrier (Figure 3). The decreasing Seebeck coefficient with increasing temperature in oxygen and air can be rationalized by a conventional semiconductor behaviour related to the number of charge carriers. The apparent increase of the Seebeck coefficient with temperature at low $p(O_2)$ is not fully understood. The importance of $V_{\text{O}}^{\bullet\bullet}$ in these BFO-rich materials is confirmed by the $p(O_2)$ dependence of the conductivity and the Seebeck coefficient. It is proposed that V_{Bi}^{\bullet} are also an important point defect, but further work must be carried out to quantify the concentration of the cation vacancies.

The behaviour of the conductivity shown in Figure 2 illustrates that the sintering atmosphere during fabrication of the ceramics is important for the conductivity, which falls in line with previous reports showing that conductivity can be reduced significantly by annealing in an inert or reducing atmosphere.²¹ Although the results presented herein are on BKT substituted BFO, we propose that the present observations gives valuable insight for the thermal evolution of the electrical conductivity of bulk pure BFO.²²⁻²⁵

The ferroelectric phase transition temperature of 0.8BFO and 0.9BFO was determined by three different methods in reasonable agreement. The Curie temperature decreases with decreasing BFO content in $(1-x)\text{BFO} - x\text{BKT}$ as shown in Figure 8. T_C for 0.8BFO and 0.9BFO are still high leaving these materials interesting for high temperature applications. T_C is at the level of pure BKT for $x \sim 0.4$, where a relaxor-type behaviour has been reported for pseudo cubic $(1-x)\text{BFO} - x\text{BKT}$ solid solutions.^{17,21}

The relaxation time for the red-ox driven point defect equilibria can be qualitatively derived from the DC conductivity and thermopower measurements although this was not the primary goal of the experiments. The electrical relaxation for 0.9BFO at 700 °C are shown in Figure 9a where the normalized conductivity upon switching between O_2 and synthetic air are given as function of time.

The relaxation time for oxidation and reduction was found to be comparable. The relaxation is an activated process and the relaxation time increases significantly with decreasing temperatures as illustrated by the relaxation curve at 550 °C, also depicted in Figure 9a. The rapidly increasing relaxation time with decreasing temperature is in good agreement with similar data reported for 0.7BFO-0.3BKT by Morozov et al.²⁰ An important observation is the immediate response from the material to a shift in the atmosphere, even at 550 °C, implying significant mobility of point

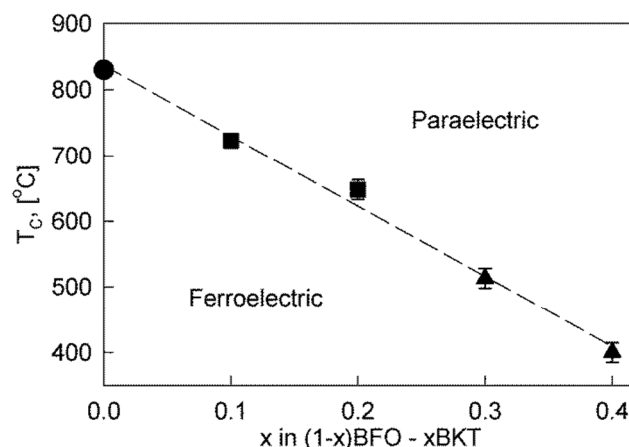


Fig 8 The Curie temperature as a function of BFO-content in $(1-x)\text{BFO} - x\text{BKT}$. Squares from this work (DTA), circle⁷ and triangles²¹ from elsewhere. Dashed line is a guide to the eye.

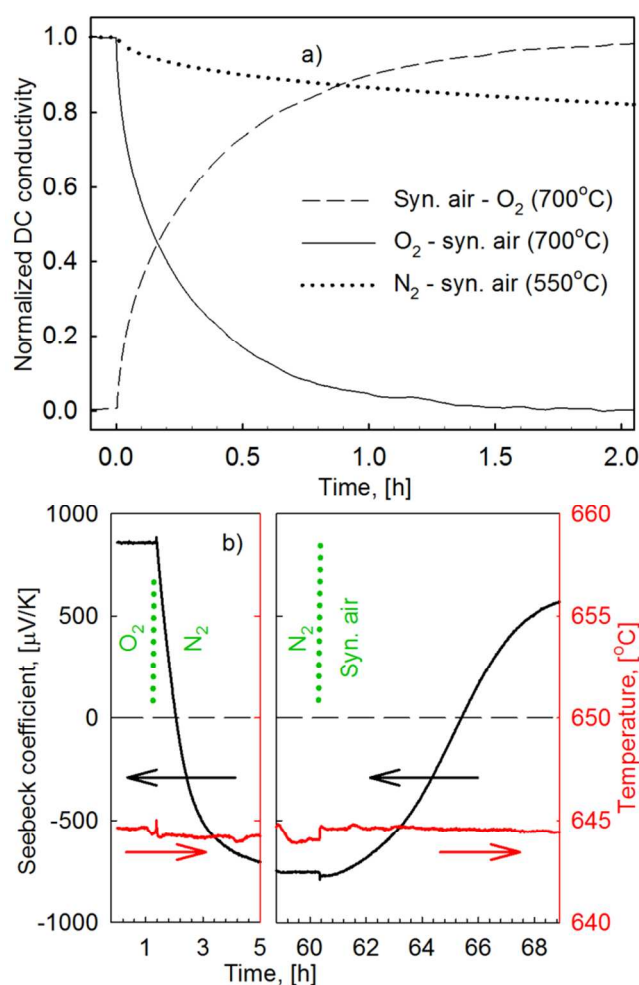


Fig 9 a) The relaxation of normalized conductivity upon switching between O_2 and synthetic air at 700 °C for 0.9BFO. Also shown is relaxation upon a shift from N_2 to synthetic air at 550 °C. b) The material response for the Seebeck coefficient upon switching atmospheres from O_2 via N_2 to synthetic air at 650 °C (0.9BFO).

Table 2 Mobility of electrons and holes respectively used in the point defect model, and thermodynamic data for the point defect reactions for 0.8BFO and 0.9BFO

| | Temperature | μ_e | μ_h | $\Delta_f H$ (eq. 4) | $\Delta_f S$ (eq. 4) | $\Delta_f G$ (eq. 4) | $\Delta_f H$ (eq. 5) | $\Delta_f S$ (eq. 5) | $\Delta_f G$ (eq. 5) |
|--------|-------------|------------------------|------------------------|-------------------------|-------------------------|-------------------------|-------------------------|-------------------------|-------------------------|
| | [°C] | [cm ² /V/s] | [cm ² /V/s] | [kJ/mol] | [J/mol] | [kJ/mol] | [kJ/mol] | [J/mol] | [kJ/mol] |
| 0.8BFO | 700 | 0.052 | 0.050 | -343 | -130 | -216 | -28 | -130 | 99 |
| | 750 | 0.054 | 0.074 | | | -210 | | | 105 |
| | 800 | 0.056 | 0.107 | | | -203 | | | 112 |
| 0.9BFO | 700 | 0.046 | 0.030 | -340 | -130 | -213 | -31 | -130 | 96 |
| | 750 | 0.047 | 0.063 | | | -207 | | | 102 |
| | 800 | 0.056 | 0.107 | | | -200 | | | 109 |

defects at temperatures significantly below T_C . Fast relaxation was also observed during measurements of the Seebeck coefficient (Figure 9b). The figure shows the reversible response going from p-type (in O_2) via n-type (in N_2) and back to p-type (in synthetic air) semiconductor behaviour.

The hardness of ferroelectric PZT can be tuned by acceptor and donor substitution,^{49,50} and the hardening of acceptor doped PZT has been explained by defect ordering due to rearrangement of oxygen vacancies.⁵¹ Such ordering has also been studied in e.g. BaTiO₃ by long term aging at elevated temperatures ($<T_C$).⁵² The driving force for point defect ordering and the formation of “defect dipoles” is minimization of electrostatic and probably also elastic energy that arises below T_C . Above T_C the material will have a paraelectric centro-symmetric structure with no driving force for ordering of charged point defects. Below T_C , a spontaneous polarization develops and the point defects will energetically prefer specific sites and form i.e. defect dipoles. These ordered defects subsequently act as effective pinning centres for domain wall movement.⁵² The hard ferroelectric characteristics of BFO have been related to point defects, though the mechanism is not yet clear.⁴ Because the T_C of BFO is 830 °C, the driving force for point defect ordering will emerge already at high temperatures ($<T_C$). It is evident from the electrical relaxation curves shown in Figure 9a that there is significant oxygen ion mobility at temperatures as low as 550 °C. Since these measurements were performed on bulk materials, the diffusion length scale of the process involving a shift in the conductivity is on an mm scale.⁵³ The length scale of oxygen vacancy diffusion required for defect dipole formation is only within a unit cell. It is therefore reasonable to assume that oxygen vacancy mobility is sufficient at temperatures much lower than 550 °C. This is important because defect ordering in high T_C materials will start immediately below T_C if the point defects are sufficiently mobile. The high T_C of these materials and the mobility, evidenced by the relaxation data, show that point defect ordering likely occurs in BFO materials, possibly explaining the hard ferroelectric properties reported for these materials.⁴

The unit cell volume of $(1-x)\text{BFO} - x\text{BKT}$ decreases with the addition of BKT, along with a decreasing lattice distortion (c_p/a_p , Figure 6). The lattice distortion of 1.0BFO,⁴⁶ 0.9BFO and 0.8BFO is ~1.015, 1.013 and 1.009, respectively. The large intrinsic lattice distortion (strain) observed for 1.0BFO is one factor contributing to the large piezoelectric response observed. The large strain in BFO may cause problems with the mechanical performance. Introduction of BKT not only reduces the challenges with secondary phases during synthesis but do also offer the possibility to adjust T_C as well as the crystallographic strain. $(1-x)\text{BFO} - x\text{BKT}$ becomes pseudo

cubic $x \sim 0.4$ which implies that most of the lattice distortion is suppressed by substitution, hence a low BKT content is preferable.¹⁷ On the other hand, a low polarization and strain response to an applied DC electric field was observed for $x < 0.4$. This reflects the hard ferroelectric characteristics of BFO challenging a wider application of BFO as a piezoelectric or ferroelectric material.¹⁰ The understanding of the point defect chemistry presented herein offers a path to understand both hardening of BFO as well as to reduce the electrical conductivity and thereby the dielectric loss.

Finally, we address the relation of the major charge carriers and charged domain walls in BFO.^{4,54,55} The conductivity along 71° domain walls has been described as n-type⁵⁵ (La-substituted BFO) and the concentration of oxygen vacancies has been shown to influence the domain wall conductivity⁵⁴ (pure BFO). The work described herein shows that both p- and n-type behaviour and electrical conductivity easily can be changed by annealing in different partial pressures of oxygen. The point defect equilibria, controlling the valence of Fe, can also be influenced by strain as recently shown for $\text{CaMnO}_{3-\delta}$.⁵⁶ The thermal processing of BFO, also in case of BFO thin films, may therefore strongly affect the electrical properties.

5. Conclusions

A minimum in the DC electrical conductivity of 0.8BFO and 0.9BFO was observed as a function of $p(\text{O}_2)$, which reflects a shift from p-type to n-type conductivity upon decreasing the partial pressure of oxygen. The change of the majority charge carrier was confirmed by the change of the sign of the Seebeck coefficient measured in different atmospheres. The conductivity was successfully described by a conventional mass action type point defect model with electrons and holes as major charge carriers and oxygen vacancies and A-site vacancies as additional point defects. A high Curie temperature of BFO was retained with the introduction of 10 and 20 mol% BKT, and the ferroelectric to the paraelectric phase was established by a combination of dielectric spectroscopy thermal analysis and high temperature XRD.

Acknowledgements

The Research Council of Norway (FRINATEK project no. 197497/F20) is acknowledged for financial support. We acknowledge discussion concerning the interpretation of the data with Dr. Maxim Morozov.

Physical Chemistry Chemical Physics Accepted Manuscript

Notes and references

^a Department of Materials Science and Engineering, Norwegian University of Science and Technology, Trondheim, 7491 Trondheim, Norway E-mail: grande@ntnu.no.

- 1 European Parliament, C. Off. J. Eur. Union 2011, **54** (L174), 89.
- 2 J. Rodel, W. Jo, K. T. P. Seifert, E. M. Anton, T. Granzow and D. Damjanovic, *J. Am. Ceram. Soc.*, 2009, **92**, 1153.
- 3 G. Catalan and J. F. Scott, *Adv. Mater.*, 2009, **21**, 2463.
- 4 T. Rojac, A. Bencan, B. Malic, G. Tutuncu, J. L. Jones, J. E. Daniels and D. Damjanovic, *J. Am. Ceram. Soc.*, 2014, **97**, 1993.
- 5 T. Rojac, M. Kosec and D. Damjanovic, *J. Am. Ceram. Soc.*, 2011, **94**, 4108.
- 6 D. Lebeugle, D. Colson, A. Forget and M. Viret, *Appl. Phys. Lett.*, 2007, **91**, 022907.
- 7 R. Palai, R. S. Katiyar, H. Schmid, P. Tissot, S. J. Clark, J. Robertson, S.A.T. Redfern, G. Catalan and J.F. Scott, *Phys. Rev. B*, 2008, **77**, 014110.
- 8 S. Selbach, M.-A. Einarsrud and T. Grande, *Chem Mater.*, 2009, **21**, 169.
- 9 M. Valant, A. K. Axelsson and N. Alford, *Chem. Mater.* 2007, **19**, 5431.
- 10 T. Rojac, M. Kosec, B. Budic, N. Setter and D. Damjanovic, *J. Appl. Phys.*, 2010, **108**, 074107.
- 11 Y. Hiruma, H. Nagata and T. Takenaka, *Jpn. J. Appl. Phys.*, 2007, **46**, 1081.
- 12 C. F. Buhner, *J. Chem. Phys.*, 1962, **36**, 798.
- 13 Y. Hiruma, R. Aoyagi, H. Nagata and T. Takenaka, *Jpn. J. Appl. Phys.*, 2005, **44**, 5040.
- 14 E. T. Weffring, M. I. Morozov, M.-A. Einarsrud and T. Grande, *J. Am. Ceram. Soc.*, 2014, **97**, 2928.
- 15 J. Bennett, A. J. Bell, T. J. Stevenson, R. I. Smith, I. Sterianou, I. M. Reaney and T. P. Comyn, *Mater. Lett.*, 2013, **94**, 172.
- 16 M. I. Morozov, M.-A. Einarsrud, T. Grande and D. Damjanovic, *Ferroelectrics*, 2012, **439**, 88.
- 17 M. I. Morozov, M.-A. Einarsrud and T. Grande, *Appl. Phys. Lett.*, 2012, **101**, 252904.
- 18 H. Matsuo, Y. Noguchi, M. Miyayama, M. Suzuki, A. Watanabe, S. Sasabe, T. Ozaki, S. Mori, S. Torii and T. Kamiyama, *J. Appl. Phys.*, 2010, **108**, 104103.
- 19 J. M. Kim, Y. S. Sung, J. H. Cho, J. K. Song, M. H. Kim, H. H. Chong, T. G. Park, D. Do and S. S. Kim, *Ferroelectrics* 2010, **404**, 88.
- 20 M. I. Morozov, M.-A. Einarsrud and T. Grande, *Appl. Phys. Lett.*, 2014, **104**, 122905.
- 21 M. I. Morozov, M.-A. Einarsrud and T. Grande, *J. Appl. Phys.* 2014, **115**, 044104.
- 22 T. R. Paudel, S. S. Jaswal and E. Y. Tsymlal, *Phys. Rev. B.*, 2012, **85**, 104409.
- 23 A. S. Poghosian, H. V. Abovian, P. B. Avakian, S. H. Mkrtchian and V. M. Haroutunian, *Sens. Actuator. B-Chem.* 1991, **4**, 545.
- 24 Z. Dai and Y. J. Akishige, *Phys. D: Appl. Phys.*, 2010, **43**, 445403.
- 25 Z. Zhang, P. Wu, L. Chen and J. L. Wang, *Appl. Phys. Lett.*, 2010, **96**, 232906.
- 26 N. Maso and A. R. West, *Chem. Mater.*, 2012, **24**, 2127.
- 27 K. Kalantari, I. Sterianou, S. Karimi, M. C. Ferrarelli, S. Miao, D. C. Sinclair and I. M. Reaney, *Adv. Funct. Mater.*, 2011, **21**, 3737.
- 28 X. D. Qi, J. Dho, R. Tomov, M. G. Blamire and J. L. MacManus-Driscoll, *Appl. Phys. Lett.*, 2005, **86**, 062903.
- 29 K. Abe, N. Sakai, J. Takahashi, H. Itoh, N. Adachi and T. Ota, *Jpn. J. Appl. Phys.*, 2010, **49**, 09MB01.
- 30 Y. Wang and N.-W. Nan, *Appl. Phys. Lett.*, 2006, **89**, 052903.
- 31 M. C. Li and J. L. MacManus-Driscoll, *Appl. Phys. Lett.*, 2005, **87**, 252510.
- 32 S. Hunpratub, P. Thongbai, T. Yamwong, R. Yimnirun and S. Maensiri, *Appl. Phys. Lett.*, 2009, **94**, 062904.
- 33 X. D. Qi, J. Dho, R. Tomov, M. G. Blamire and J. L. MacManus-Driscoll, *Appl. Phys. Lett.*, 2005, **86**, 062903.
- 34 V. L. Kozhevnikov, I. A. Leonidov, M. V. Patrakeev, E. B. Mitberg and K. R. Poeppelmeier, *J. Solid State Chem.*, 2001, **158**, 320.
- 35 J. Mizusaki, M. Yoshihiro, S. Yamauchi and K. Fueki, *J. Solid State Chem.*, 1985, **58**, 257.
- 36 J. Mizusaki, T. Sasamoto, W. R. Cannon and H. K. Bowen, *J. Am. Ceram. Soc.*, 1982, **65**, 363.
- 37 T. Arakawa, S. Tsuchi-ya and J. Shiokawa, *Mater. Res. Bull.*, 1981, **16**, 97.
- 38 M. Siemons, A. Leifert and U. Simon, *Adv. Funct. Mater.*, 2007, **17**, 2189.
- 39 I. Waernhus, P. E. Vullum, R. Holmestad, T. Grande and K. Wiik, *Solid State Ionics*, 2005, **176**, 2783.
- 40 *Topas*, 4.2 Bruker AXS: 2009.
- 41 S. M. Selbach, T. Tybell, M.A. Einarsrud and T. Grande, *Phys. Rev. B*, 2009, **79**, 214113.
- 42 S. M. Selbach, T. Tybell, M.-A. Einarsrud and T. Grande, *Chem. Mater.*, 2009, **21**, 5176.
- 43 P. V. B. Rao, E. V. Ramana and T. B. Sankaram, *J. Alloy Compd.* 2009, **467**, 293.
- 44 T. Yokota, R. Aoyagi and M. Gomi, *J. Ceram. Soc. Jpn.*, 2013, **121**, 675.
- 45 D. C. Arnold, K. S. Knight, G. Catalan, S. A. T. Redfern J. F. Scott, P. Lightfoot and F. D. Morrison, *Adv. Funct. Mater.*, 2010, **20**, 2116.
- 46 S. M. Selbach, T. Tybell, M.-A. Einarsrud and T. Grande, *Adv. Mater.*, 2008, **20**, 3692.
- 47 M. Christensen, Master thesis, Norwegian University of Science and Technology, Trondheim, Norway, 2013.
- 48 E. Bakken, T. Norby and S. Stolen, *J. Mater. Chem.*, 2002, **12**, 317.
- 49 M. I. Morozov and D. Damjanovic, *J. Appl. Phys.*, 2008, **104**, 034107.
- 50 M. I. Morozov and D. Damjanovic, *J. Appl. Phys.*, 2010, **107**, 034106.
- 51 A. Chandrasekaran, D. Damjanovic, N. Setter and N. Marzari, *Phys. Rev. B*, 2013, **88**, 214116.
- 52 X. B. Ren, *Nat. Mater.*, 2004, **3**, 91.
- 53 T. Grande, J. R. Tolchard and S. M. Selbach, *Chem. Mater.* 2012, **24**, 338.
- 54 J. Seidel, P. Maksymovych, Y. Batra, A. Katan, S. Y. Yang, Q. He, A. P. Baddorf, S. V. Kalinin, C. H. Yang, J. C. Yang, Y. H. Chu, E. K. H. Salje, H. Wormeester, M. Salmeron and R. Ramesh, *Phys. Rev. Lett.*, 2010, **105**, 197603.
- 55 S. Farokhipoor and B. Noheda, *Phys. Rev. Lett.*, 2011, **107**, 127601.

- 56 U. Aschauer, R. Pfenninger, S. M. Selbach, T. Grande and N. A. Spaldin, *Phys. Rev. B*, 2013, **88**, 054111.